IEEE Access
Multidisciplinary ⋮ Rapid Review ⋮ Open Access Journal

Received October 23, 2021, accepted November 7, 2021, date of publication November 9, 2021,
date of current version November 23, 2021.

Digital Object Identifier 10.1109/ACCESS.2021.3126700

The Use of a Pair of 3D-Printed Near Field Superstructures to Steer an Antenna Beam in Elevation and Azimuth

TOUSEEF HAYAT[1], (Student Member, IEEE), MUHAMMAD U. AFZAL[2], (Senior Member, IEEE), FOEZ AHMED[2], (Student Member, IEEE), SHIYU ZHANG[3], (Member, IEEE), KARU PRIYATHAMA ESSELLE[2] (Fellow, IEEE), AND J. VARDAXOGLOU[3], (Fellow, IEEE)

[1]School of Engineering, Macquarie University, Sydney, NSW 2109, Australia
[2]School of Electrical and Data Engineering, University of Technology Sydney, Ultimo, NSW 2007, Australia
[3]Wolfson School of Mechanical, Electrical and Manufacturing Engineering, Loughborough University, Loughborough LE11 3TU, U.K.

Corresponding author: Touseef Hayat (touseef.hayat@mq.edu.au)

This work was supported in part by the Australian Research Council Discovery Grant, in part by the International Macquarie University Research Excellence Scholarship (iMQRES) under Grant 2017062/20181097, in part by the University of Technology Sydney Seed Grant, and in part by the University of Technology Sydney International Research Scholarship.

ABSTRACT The paper presents a method to design beam-steering antennas using a pair of 3D printed perforated dielectric structures (PDSs) placed in the near-field region of a base antenna, which has a fixed beam. Detailed designs and quantitative comparison of two beam-steering antenna systems are presented. One antenna system has a conical horn antenna and the other uses a resonant-cavity antenna (RCA) as the base antenna. In both cases, the first PDS transforms the phase distribution of the aperture near field and hence tilts the antenna beam to an offset angle. The second PDS, placed above the first, introduces an additional linear progression to the phase of the near field. The two PDSs are rotated independently to steer the beam in both azimuth and elevation. The PDSs have been 3D-printed using acrylonitrile butadiene styrene (ABS) filaments. Each prototype was fabricated in about 16 hours, weighs 300 grams, and costs approximately 5.5 US Dollars. The measured results show that, at the operating frequency of 11 GHz, the RCA-based system has a peak gain of 17.7 dBi compared to the 16.6 dBi gain obtained with the horn-based system. In a fixed E-plane, the variation in the aperture near-field phase of the horn antenna (115°) is much less than that of the RCA (360°). This reduces the efforts required for phase correction and hence led to the former having a larger 3dB measured gain bandwidth of 1.2 GHz compared with the 0.7 GHz bandwidth of the latter, but at the cost of 35.6% increase in the total height of the antenna system.

INDEX TERMS Acrylonitrile butadiene styrene, additive manufacturing, beam steering, meta-steering, near field, non-homogenous, phased array, rapid prototyping, reconfigurable antennas, resonant-cavity antenna, transmission phase delay.

I. INTRODUCTION

Beam-steering is one of the most desired characteristics of front-end antennas required for communications, radar, and remote sensing systems [1]–[3]. It is one of the main features of 5G communications systems, to mitigate inherent limitations of path loss, obstacle attenuation, and misalignment due to wind sway [4]–[7]. Continuous beam-steering technologies are also pivotal for the success of communication systems with mobile transmitter or receivers [8], [9].

There exist several high-gain antenna beam-steering technologies [10], [11]. The popular electronic beam-steering antenna systems, designed using phase shifters, are expensive for some wireless applications [12], [13]. On the other hand, beam-steering antenna systems that involve mechanical tilting of a reflector antenna or a flat-panel antenna are also expensive due to the required motion in three-dimensional space (tilting and rotation) to steer the beam [4].

The associate editor coordinating the review of this manuscript and approving it for publication was Weiren Zhu.

A low-cost and rapidly coinable beam-steering antenna technology is desirable for price-sensitive consumer markets.

A relatively new method of steering a high-gain antenna beam by rotating a pair of metasurfaces in the near-field region of a fixed base antenna has attracted significant attention of the research community [14]–[16]. Also known as Near-Field Meta-Steering, this method has the potential to deliver medium-to-high gain antennas for a range of applications. However, the early development focused on demonstrating the concept by using multilayered printed metasurfaces, which have a large price tag associated with the material and fabrication [4], [17], [18].

The two phase transformation metasurfaces in a Near-Field Meta-Steering system can be replaced with two dielectric wedges or two stepped dielectrics, which can be fabricated using dielectric blocks or 3D printing of plastics [19], [20]. Nevertheless, this is only feasible for antenna systems with low to medium gain and a small aperture. The resulting structure is both complicated and fragile when it comes to medium-to-high-gain large aperture antennas [21], [22]. A dielectric wedge maintains a constant slope and can be extremely thick on one side relative to the other. This disparity in heights at two ends makes it difficult to rotate. A concept called 'phase wrapping' can be used to create a sawtooth-shaped structure that reduces the maximum height of the wedge but compromises the structural integrity of the structure because of extremely small thickness at each wrapping point [23]. These phase-wrapped versions of dielectric wedges, additionally, suffer from shadowing effects due to their non-planar geometry [22].

To address the limitations of such wedge-based beam-steering antennas, this paper presents two antennas with planar perforated dielectric structures (PDSs). Each PDS is a cylinder with different sizes of square perforations distributed throughout the structure. Each PDS has planar constant-height geometry and hence does not suffer from shadowing effect even when applied for large aperture antennas where multiple wrapping points exist. The two PDSs have been designed so that they can be 3D printed using simple printers, to leverage on low-cost advantage of this technology. The maximum perforation size in the PDSs is kept within a safe limit in the design process to ensure that the structure is structurally rigid and suitable even for harsh mobile environments.

The PDSs presented here have square perforations that offer a wider transmission phase range when compared with traditional circular perforations [24]. The PDSs were fabricated in a single step using 3D printing; bonding or soldering is not required for their fabrication. Both PDSs were developed from one kg spool of Acrylonitrile butadiene styrene (ABS) filament that costs around US$ 16.30. The alternate low-cost candidates for design of PDSs are Polylactic Acid (PLA), High Impact Polystyrene (HIPS) and nylon filaments but ABS is particularly considered here because of its robustness and compatibility with most of the household and industrial grade 3D printers. High radio frequency (RF) loss of currently common low-cost ABS compromises antenna performance at present. Nevertheless, with advancements in Material Science, RF characteristics of 3D-printable material are improving rapidly. Already there are low-loss 3D-printable material (e.g. PREPERM®), that are economical compared to traditional dielectrics but are a lot more expensive than commonly available ABS. With time, more low-loss 3D-printable material will be available and prices will decrease, and hence the radiation performance of antennas designed following the method presented in this manuscript will improve.

The concept is demonstrated by developing two beam-steering systems, one using a resonant-cavity antenna (RCA) as the base antenna and the other using a conical horn. The paper is organized as follows. Section II describes the mechanism that is employed to steer the beam in both azimuth and elevation using a pair of PDSs. The characterization of inhomogeneous dielectric, which forms the basis of PDSs, is explained in Section III. Complete system designs are discussed in Section IV and V. Measured results and detailed performance comparison are included in Section VI. Finally, a conclusion is given in Section VII.

II. BEAM-STEERING MECHANISM

A quintessential depiction of the proposed beam-steering antenna system is given in Fig. 1. The system comprises a pair of PDSs that are placed in a near-field region of a base antenna so that the phase of the field is sequentially modified by the pair of PDSs. Each of the two PDSs introduce a linear phase-delay profile that tilts the antenna beam in a direction away from the broadside direction (i.e. z-axis). The aperture phase distribution and thus the antenna beam direction is dynamically controlled by independently rotating the two PDSs. In addition, the first PDS improves the non-uniformity existing in the near-field phase of the base antennas along with introducing the linear phase progression. It is for this reason that we refer to the lower PDS as Steering and Correction PDS (SCP). The SCP transforms the non-uniform phase distribution of the base antenna aperture by near-field phase correction and tilts the antenna beam to an offset angle δ_1. The upper PDS does the function of steering only, and thus is called Steering Only PDS (SOP). The SOP placed a fraction of a wavelength above the SCP, introduces an additional linear progression to the phase distribution of the near- field, which in the absence of the lower PDS would tilt the beam by an angle of δ_2. Each PDS in the pair can be physically rotated independently by angles α_1 and α_2 respectively, to steer the beam in both azimuth and elevation. The beam direction in the far-field region is represented by elevation and azimuth angles θ and φ, respectively. They depend on δ_1, δ_2, α_1 and α_2 and can be accurately predicted using the recently reported Phase Method [25]. The phase-delay gradient (p_i) of each PDS is related to its tilt angle according to:

$$p_i = \sin \delta_i \times k_0 \tag{1}$$

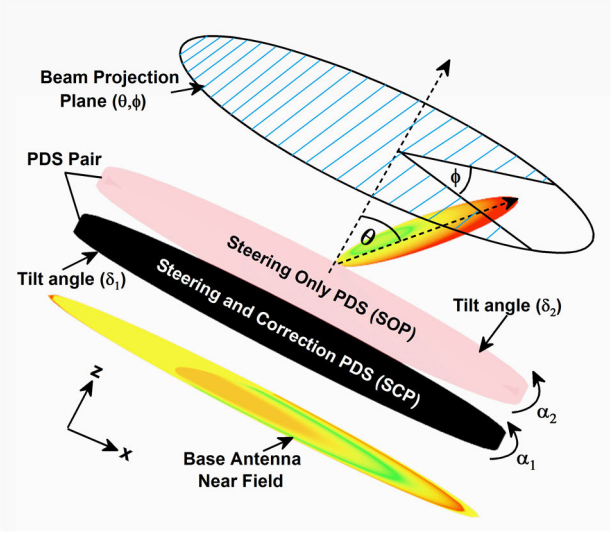

FIGURE 1. Configuration of a Near-Field Meta-Steering system comprising a pair of PDSs placed in a near-field region of a base antenna.

TABLE 1. Theoretically calculated beam direction when SCP is fixed and SOP is rotated.

α_1 (Degrees)	α_2 (Degrees)	θ (Degrees)	φ (Degrees)
0	0	48.7	0
0	30	46.2	15
0	60	40.6	30
0	90	32.1	45
0	120	22.6	60
0	150	11.2	75
0	180	0.0	90

where, k_0 is the wavenumber in free space and δ_i is the individual tilt angle of the PDS. In an antenna system that has two PDSs with the phase-delay gradients of p_1 and p_2 and that are rotated by arbitrary angles α_1 and α_2, the elevation and azimuth angles of the beam direction are given by [25]:

$$\theta = \sin^{-1}\left\{\frac{1}{k}[p_1^2 + p_2^2 + 2p_1p_2\cos(\alpha_1 - \alpha_2)]^{\frac{1}{2}}\right\} \quad (2)$$

$$\varphi = \tan^{-1}\left(\frac{p_1\sin\alpha_1 + p_2\sin\alpha_2}{p_1\cos\alpha_1 + p_2\cos\alpha_2}\right) \quad (3)$$

It can be observed that the elevation and azimuth angles of the beam direction can be independently changed dynamically by appropriate rotation of the two PDSs, as done in previous recent works [15], [20], [26].

To understand this, consider a hypothetical scenario of two PDSs, which are designed for an identical tilt angle of 22° ($\delta_1 = \delta_2 = 22°$) and at the operating frequency of 11 GHz and are placed in the near-field region of an antenna. Because of the same tilt angles, the phase delay gradients p_1 and p_2 of the two PDSs will be identical, which is equal 4.945 deg/m. The SCP is fixed along x-axis (i.e. $\alpha_1 = 0°$) and the SOP is rotated between 0° and 180° in counter-clockwise direction with a step of 60° (i.e. $\alpha_2 = 0$, 60, 120, and 180°). By substituting the values of p_1, p_2, α_1 and α_2 in equations (2) and (3), elevation (θ) and azimuth (φ) angles of the beam direction can be calculated for each orientation combination of the PDSs. The calculated azimuth and elevation angles for four different orientations of two PDSs are given in Table 1. The beam position in elevation and azimuth for different orientations of PDSs pair is illustrated in Fig. 2(a) to (d). When $\alpha_1 = \alpha_2 = 0°$, the beam is steered to $\theta = \theta_{max} = 48°$ and $\varphi = 0°$ [25], [26]. When SOP is rotated in counter-clockwise direction at $\alpha_2 = 120°$, the beam peak will be at $\theta = 22°$ and $\varphi = 60°$. The next section explains the theory of transmission phase delay through non-homogenous dielectrics, which can be arranged with gradient phase delay to design PDSs for beam-steering.

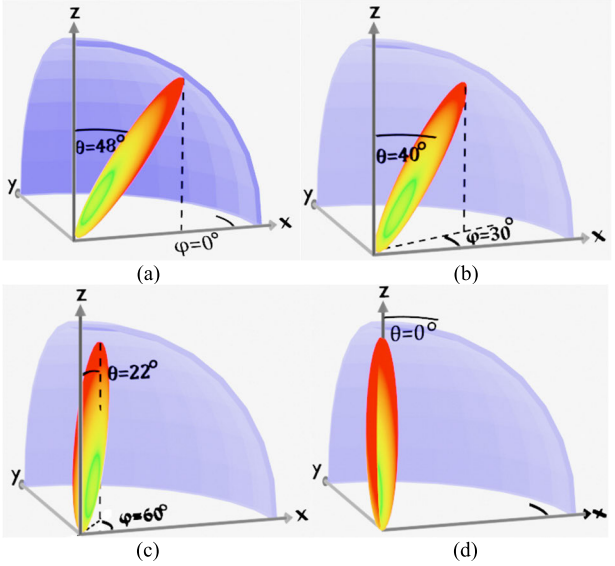

FIGURE 2. Depiction of antenna beam direction in elevation (θ) and azimuth (φ) when SCP is fixed and SOP is rotated in counter-clockwise direction at (a) $\alpha_2 = 0°$ (b) $\alpha_2 = 60°$ (c) $\alpha_2 = 120°$ and (d) $\alpha_2 = 180°$.

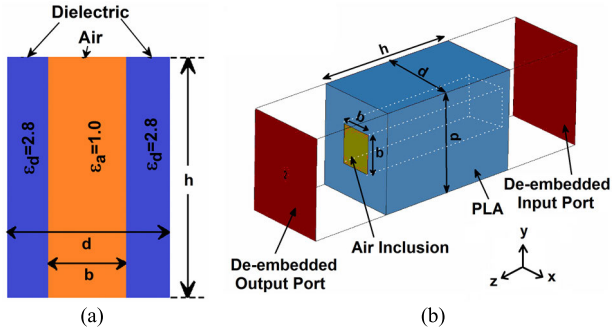

FIGURE 3. (a) Cross-sectional view of non-homogenous dielectric (b) Prospective view of dielectric block with air inclusion.

III. CARACTERISATION OF INHOMOGENOUS DIELECTRIC CELLS

The PDSs of the proposed beam-steering antenna system has been implemented using 3D-printed dielectric blocks, which

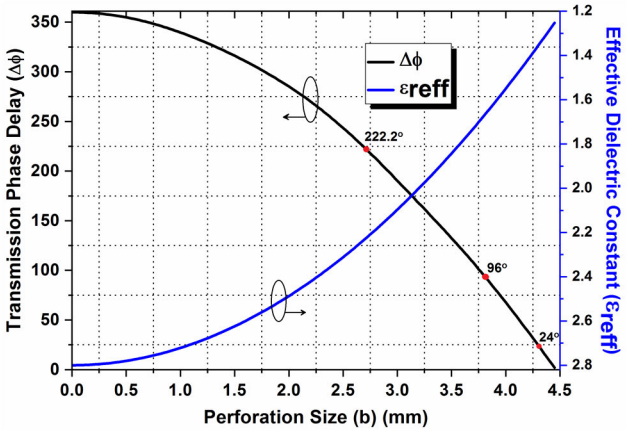

FIGURE 4. Variation in effective permittivity and transmission phase delay with change in perforation size.

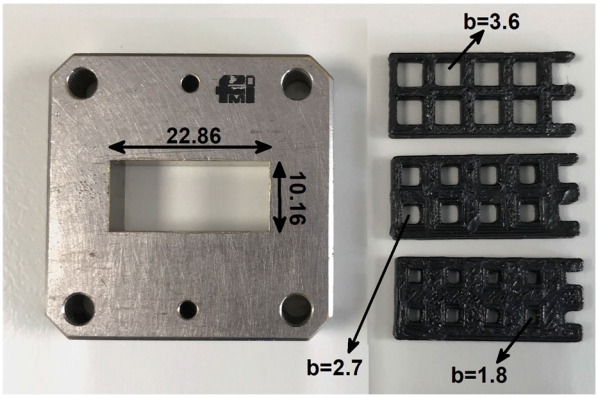

FIGURE 5. Left: WR-90 waveguide flange (sample holder). Right: three 3D- printed inhomogeneous dielectric samples.

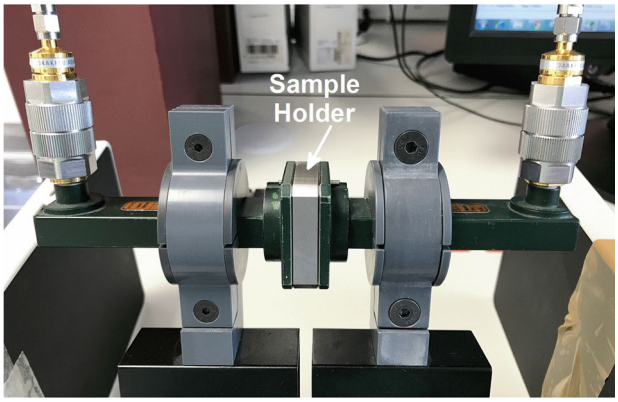

FIGURE 6. Experimental setup for Nicolson-Ross Weir transmission reflection coefficient measurements of samples.

are made of inhomogeneous cells. A 3D model of an inhomogeneous cell used here is shown in Fig. 3. It is a rectangular prism of ABS plastic with square base of size $d \times d$ and height h. The dielectric constant of the ABS material is 2.8 [24], [27]. Note that there is a square-shaped air-filled hole with dimensions of $b \times b$ in the middle of the cell. The effective relative permittivity (ε reff) of such an inhomogeneous cell can be expressed in terms of the filling factor of dielectric (gamma), as, [28]:

$$\varepsilon_{\text{reff}} = \varepsilon_{\text{r}}\,(1-\gamma) + \gamma \tag{4}$$

where, γ is the filling factor given by [24], [27], [28]:

$$\gamma = \frac{\text{A}_{\text{o}}}{\text{A}} = \frac{\text{b}^2}{\text{d}^2} \tag{5}$$

where, A_{o}, is the area of the perforation, and A is the area of the unit cell. Hence the effective dielectric constant of this cell is:

$$\varepsilon_{\text{reff}} = \varepsilon_{\text{r}}\left(1 - \frac{\text{b}^2}{\text{d}^2}\right) + \frac{\text{b}^2}{\text{d}^2} \tag{6}$$

As an example, consider a specific unit cell with lateral dimensions (periodicity d) of 4.8 mm. Fig. 4 shows how the effective dielectric constant of this unit cell decreases, when b is increased from 0 and 4.5 mm.

These theoretical calculations were validated by measuring 3D-printed ABS samples with variable perforation sizes using Nicolson-Ross Weir method. Three samples with perforation lengths (b) of 1.8 mm, 2.7 mm and 3.6 mm were 3D-printed to fit the internal dimensions (22.86 mm × 10.16 mm) of the WR-90 waveguide sample holder shown in Fig. 5. Waveguide setup measurement was conducted to record complex reflection and transmission coefficients of the samples using E4991A impedance analyser in the frequency band between 9 GHz and 11.5 GHz. A photograph of the measurement setup used for the s-parameter retrieval is shown in Fig. 6. This custom-built setup has a pair of waveguides at the two ends and the sample under test is placed inside the sample holder (waveguide flange). Flanges have standard dimensions, which correspond to the waveguide pair used for measurement setup. The effective dielectric constant of samples was determined from measured s-parameters using the method described in [29]. The measured effective dielectric constants and loss tangents of all three samples are shown in Fig. 7. Theoretically calculated and measured values of effective dielectric constant in Fig. 7 are in good agreement for all three perforation sizes tested.

After experimental validation of the effective dielectric constant of inhomogeneous cells, their transmission phase characteristics were investigated. Cells with varying perforations were modelled with periodic boundary conditions in Computer Simulation Technologies (CST) Microwave Studio and full-wave simulations were conducted to predict its transmission characteristics at the operating frequency of 11 GHz. The transmission-phase delay predicted for the unit cell is depicted by the black curve in Fig. 4. As expected, the transmission-phase delay is maximum for the solid dielectric that has no perforation and it decreases with the increase of perforation size. This transmission-phase data have been used to design the PDSs as described in the following section.

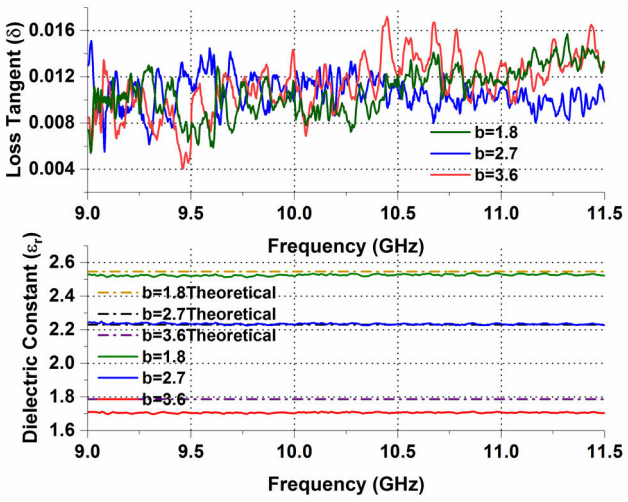

FIGURE 7. Loss tangent and effective dielectric constant of three different samples measured in a wider frequency range around the centre operating frequency.

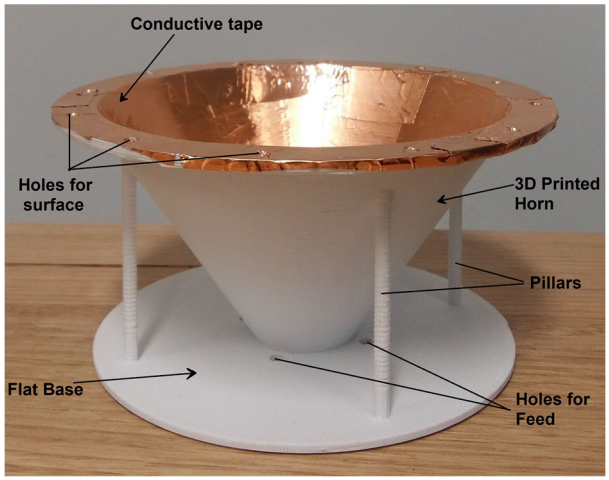

FIGURE 8. The 3D printed horn antenna where inner surfaces are covered with copper tape.

IV. SYSTEM I: BEAM-STEERING SYSTEM WITH A 3D-PRINTED CONICAL HORN BASE ANTENNA

Although any type of base antenna can be used to authenticate the working principle of PDSs, in this paper we focus on two specific types of base antennas, a conical horn antenna and a classical resonant-cavity antenna (RCA), because both of them have simple configurations. The two systems, which are referred to as System I and System II, respectively, were designed, prototyped and measured, and their performance was analysed after post-processing the near-field data. All components of the system were designed to operate at 11 GHz ($\lambda_0 = 27.3$ mm).

A. CONICAL HORN DESIGN

Our low-cost horn antenna comprises a cone that is 3D-printed out of ABS filament, as shown in Fig. 8. Its aperture diameter is 115.2 mm and height is 70.1 mm. It has a 2 mm thick circular base plate to securely fix it to a WR-75 waveguide feed at the bottom, and a circular extension on top to accommodate screws to hold the pair of PDSs for beam-steering. The four cylindrical pillars, shown in the figure, are to improve the mechanical strength of the structure. The conical horn antenna was designed and analyzed using CST Microwave Studio (MWS). The design file was exported in STL (Standard Tessellation Language) format and was converted into G-code using Simplify3D software for 3D printing. This software estimated a print time of 7 hours and consumption of 67.45 m of 1.75 mm diameter ABS filament in an Omni3D printer, which has a nozzle diameter of 0.4 mm. The extruder temperature was 240°C, the bed temperature was 110°C, and the layer height was fixed to 0.2 mm for printing. The enclosed chamber feature of the printer was availed to avoid environmental effects on printing. The fabricated prototype weighs 179g, which corresponds to an equivalent material cost of US$ 3. After printing, the inner surface of the horn was covered with conductive Copper tape. This procedure yielded a rapidly prototyped, low-cost horn antenna, whose measured performance is comparable to that of off-the-shelf expensive products available in the market [30]. The conductive tape covering is significant for the radiation performance of the horn antenna and the external 3D-printed dielectric material has no impact on radiation performance. So, it is possible to use any low-cost 3D printable plastic or polymer such as PLA, ASA, HIPS or nylon for this purpose. ABS was selected here because it is commonly available, easily printable and has the lowest cost [31].

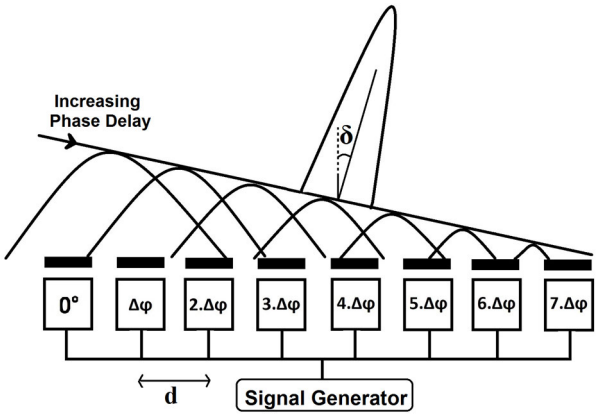

FIGURE 9. A depiction of 1D phased array fed with an increasing phase delay along the length of the array.

B. STEERING ONLY PDS (SOP)

The SOP has been designed by integrating inhomogeneous unit cells described in Section II. Its diameter is the same as that of horn (115.2 mm∼4.2λ0). The cells are spatially arranged to produce a phase delay gradient parallel to the x-axis as shown in Fig. 9. Since the length of a cell is 4.8 mm, the superstructure has of 24 cells along its diameter. According to phased array theory, The explicit mathematical

TABLE 2. Desired phase delay, effective dielectric constant and the size of air inclusion for each cell in the SOP.

N	Required Phase Delay ($\Delta\varphi$) (degrees)	Effective Dielectric Constant (ε_{reff})	Perforation length (b) (mm)
1	288	2.48	2.0
2	312	2.50	1.6
3	336	2.71	1.1
4	360 (0)	2.8	0.0
5	24	1.36	4.3
6	48	1.49	4.1
7	72	1.57	3.95
8	96	1.59	3.8
9	120	1.78	3.6
10	144	1.90	3.4
11	168	2.00	3.2
12	192	2.09	3.0
13	216	2.21	2.75
14	240	2.27	2.5
15	264	2.40	2.25
16	288	2.49	2.0
17	312	2.50	1.6
18	336	2.71	1.1
19	360 (0)	2.72	0.0
20	24	1.36	4.3
21	48	1.49	4.1
22	72	1.57	3.95
23	96	1.59	3.8
24	120	1.78	3.6

relationship to determine the phase delay gradient between two adjacent cells that is required to tilt the beam by angle of delta is [25]:

$$p = \sin\delta \times k_0 \tag{7}$$

The SOP was designed to tilt the broadside beam at an angle of 22° ($\delta = 22°$). Substituting this delta and $\lambda_0 = 27.3$ mm in equation (7), one finds the required progressive phase gradient (p) as 4.945 deg/m. With cell periodicity of 4.8 mm, this corresponds to an additional phase delay of ≈24° between two adjacent cells [32]. The phase delay in the SOP increases along one of the linear axes (x-axis here) and is constant along the orthogonal axis (y-axis here).

The Table 2 lists the column number (N) of the SOP cell (grid element) and the phase delay required ($\Delta\varphi$) through that cell in order to steer the beam to 22 degrees. The phase delay increases with a constant step and wraps back to 0° when it reaches 360°. It is to be mentioned here that the absolute phase delay in each cell is not important but the progressive phase delay change between adjacent cells is critical for steering mechanism. Hence the absolute phase delay of the first cell (N = 1) can be chosen arbitrarily. In this SOP design, phase delay of the first cell is chosen as 288° to ensure that there is no phase wrapping point in the center of the aperture.

The SOP is formed by integrating appropriate phase-shifting cells having air perforations in the dielectric, as explained in Section II. For example, to obtain a phase delay of 24°, the effective dielectric constant of the cell should be 1.36, and that requires a 4.3 mm in the cell. This is

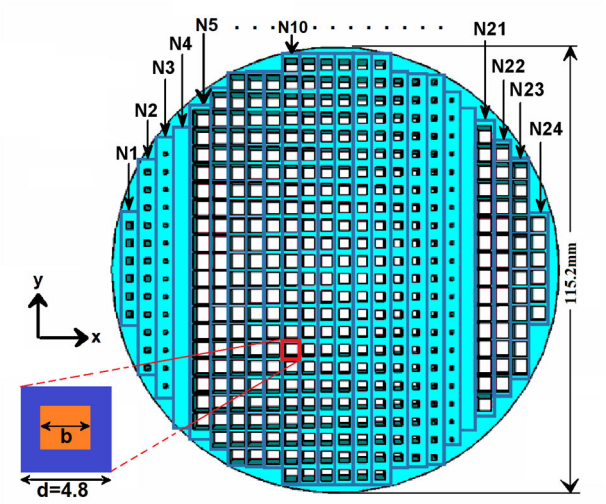

FIGURE 10. A lateral cross-section view of the beam-steering surface referred to as Steering Only PDS (SOP).

denoted by one of the red dots on the phase- delay curve in Fig. 4. Similarly, for a phase delay of 96°, a 3.8 mm perforation is required. Using this procedure, the required phase delays, effective dielectric constant values and perforation sizes of all the required 24 cells along the phase progression axis were determined and the results are listed in Table 2. The SOP was designed to be circular to match the aperture of the horn antenna. The model of the resulting SOP is shown in Fig. 10.

C. APERTURE PHASE DISTRIBUTION OF THE HORN

The SOP was designed with an assumption that the electric field at its input has a uniform phase distribution. However, it is known that the aperture phase distribution of a conical horn antenna is non-uniform. This non-uniformity. is due to the path difference from the phase centre to the edges of the cone when compared to the centre of the aperture [33]. This extra delay must be compensated for, prior to the use of SOP on top of the antenna aperture. The significance of phase correction for an antenna is that it enhances radiation characteristics of the antenna, such as gain and directivity [34].

To address this, the phase distribution of the dominant electric-field component was probed on the antenna aperture using full-wave CST simulations. To probe the phase distribution, an aperture was defined at a spacing of 13.5mm ($\lambda_0/2$) from the antenna and it was divided into a grid of 24 × 24 square cells, each having a length of 4.8 mm. The cell periodicity of 4.8 mm accommodated two phase wrapping points in the planar PDS structure of size $4.2\lambda_0 \times 4.2\lambda_0$. This highlighted the robustness of proposed PDSs over sawtooth-shaped wedges that have structural drawbacks due to wrapping points associated with them. The normalised aperture phase distribution is shown in Fig. 11. The numerical values of the probed phase at the centre of each cell along the x-axis are given in Table 3.

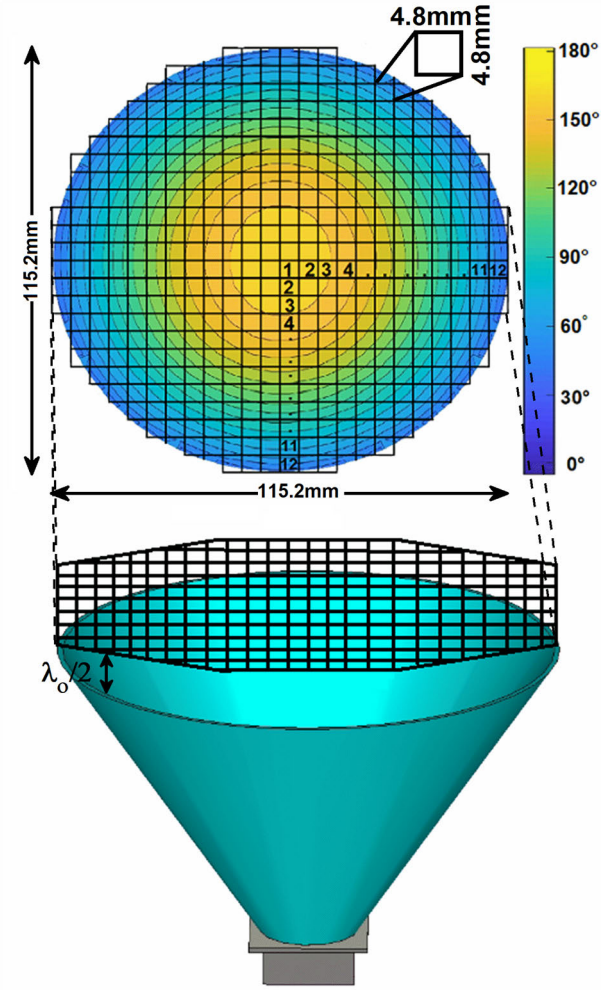

FIGURE 11. Nearly rotationally symmetrical phase distribution of the H-plane electric field on the horn aperture, predicted using CST MWS at the surface on which the dominant field was probed.

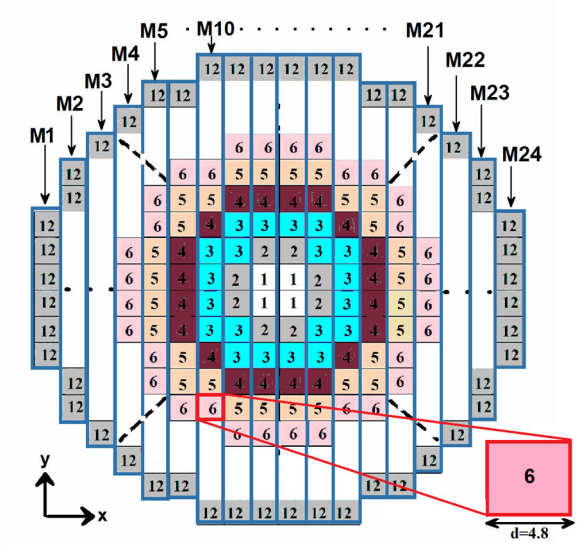

FIGURE 12. The phase delay map required to make the aperture phase distribution of the horn antenna uniform.

TABLE 3. Phase of electric field recorded and corresponding perforation sizes required in CSD to compensate error.

Segment	Aperture position along x-axis (mm)	Probed phase (deg.)	Normalized phase *(deg.)*	Correction phase delay (deg.)
1	2.4	20.6	0	171
2	7.2	11.2	-9.4	161.6
3	12	-5.3	-25.9	145.1
4	16.8	-27.6	-48.2	122.8
5	21.6	-50.1	-70.7	100.2
6	26.4	-72.2	-92.8	78.2
7	31.2	-90.6	-111.2	59.7
8	36	-104.6	-125.2	45.8
9	40.8	-122.1	-142.7	28.2
10	45.6	-146.8	-167.4	3.6
11	50.4	-140.4	-161.0	9.9
12	55.2	-127	-147.6	23.4

The phase delay required to mitigate this aperture phase non-uniformity was calculated using the detailed procedure given in [34]. Since the phase distribution is rotationally symmetrical around the centre of the aperture, the correction required in every cell also has such symmetry approximately, as depicted in the discretised map shown in Fig. 12. The required correction can be achieved with 12 discrete cells indicated in Fig. 12. The phase correction required in these twelve cells is listed in Table 3.

Once the required phase correction phase delay in each cell in Fig. 12 is calculated, it is possible to design a 3D-printed superstructure to provide the required phase correction. But that approach is undesirable, because it will increase the antenna system height and unnecessarily deteriorates the antenna performance. Instead, here these correction phase delay is incorporated to the lower PDS such that it provides both functions of phase correction and beam-steering. It is for this reason the lower PDS is referred to as the Steering and Correction PDS (SCP). The design of the SCP for the horn antenna is explained in the next sub-section.

D. STEERING AND CORRECTING PDS (SCP) DESIGN AND FABRICATION

Since the SCP produces a linear phase progression and additionally compensates for the phase non-uniformity in the aperture, its phase delay is simply the sum of the phase delay required for an SOP (described in Sub- Section *B*) and the delay required for phase correction (described in Sub-Section *C*). By combining both phase values in local unit-cells of structure, the designed SCP will have prowess to simultaneously rectify non-uniform antenna response and tilt it to an offset angle of 22°. To understand this, let us consider one of the cells close to the middle of the aperture in the 2D grid.

In SOP, the cell in column 'N10' and 17th row from the top, shown in the inset in Fig. 10, has a phase delay of 144°. The corresponding cell in the phase correcting structure is in column 'M10' and 17th row (shown in the inset in Fig. 12) and it has a phase delay of 78.2°. Hence the resultant phase delay

TABLE 4. Details for one column of cells in the CSD.

Row #	Phase delay for steering N10 value ($\Delta\varphi$)	Corr. seg. From M10	Phase delay for correction (deg.)	Total phase delay (deg.)	Perforation length (b) (mm)
1	144	12	23.4	167.4	3.2
2	144	11	9.9	153.9	3.3
3	144	10	3.6	147.6	3.4
4	144	9	28.2	172.2	3.15
5	144	8	45.8	189.8	3.0
6	144	7	59.7	203.7	2.9
7	144	7	59.7	203.7	2.9
8	144	6	78.2	222.2	2.7
9	144	5	100.2	244.2	2.5
10	144	4	122.8	266.8	2.25
11	144	3	145.1	289.1	1.95
12	144	3	145.1	289.1	1.95
13	144	3	145.1	289.1	1.95
14	144	3	145.1	289.1	1.95
15	144	4	122.8	266.8	2.25
16	144	5	100.2	244.2	2.5
17	144	6	78.2	222.2	2.7
18	144	7	59.7	203.7	2.9
19	144	7	59.7	203.7	2.9
20	144	8	45.8	189.8	3.0
21	144	9	28.2	172.2	3.15
22	144	10	3.6	147.6	3.4
23	144	11	9.9	153.9	3.3
24	144	12	23.4	167.4	3.2

of the corresponding cell in SCP is 222.2° (=144 + 78.2). The phase delays of corresponding cells were so combined throughout the aperture, in the 2D planes but the results are given in Table 4 for only one column of cells. The phase delays of all the cells in column N10 of SOP in Fig. 10 and column M10 of the correction delay map in Fig. 12 are listed in Table 4. Like all other columns, the N10 column in SOP has the same phase delay throughout the column i.e. 144° (from Table. 2) while the corresponding correction cells in M10 have varying phase delays that are given in the fourth column of Table 4. After calculating the total phase delay required in all cells of the SCP, it is formed by integrating the correct phase –shifting cells as explained in the previous sections. As an example, the net phase delay of 222.2° required through the previously discussed cell can be achieved using a 2.7 mm perforation (Fig. 3). The top view of the SCP design is shown in Fig. 13. Obviously its perforation pattern is different to that of the SOP shown in Fig. 9.

This SCP design was 3D-printed using print settings similar to those used for printing the cone of the horn. The total print time for SCP was 16 hours and 11 minutes. During the process, 146.1 m of filament length was consumed, which corresponds to a plastic weight of 369 gm and material cost of US $5.5. A circular base of uniform 4 mm thickness was printed around SCP prior to printing. Twelve holes were introduced in .stl file to accommodate spacers that hold the antenna and the superstructures together.

To test the beam-steering, the SOP designed in Sub section *B* was also fabricated using the same print settings and the

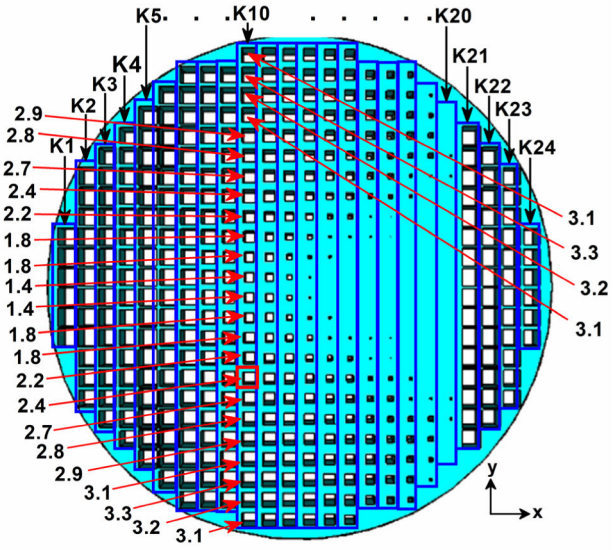

FIGURE 13. SCP designed by combining phase correction delays and phase progression delays.

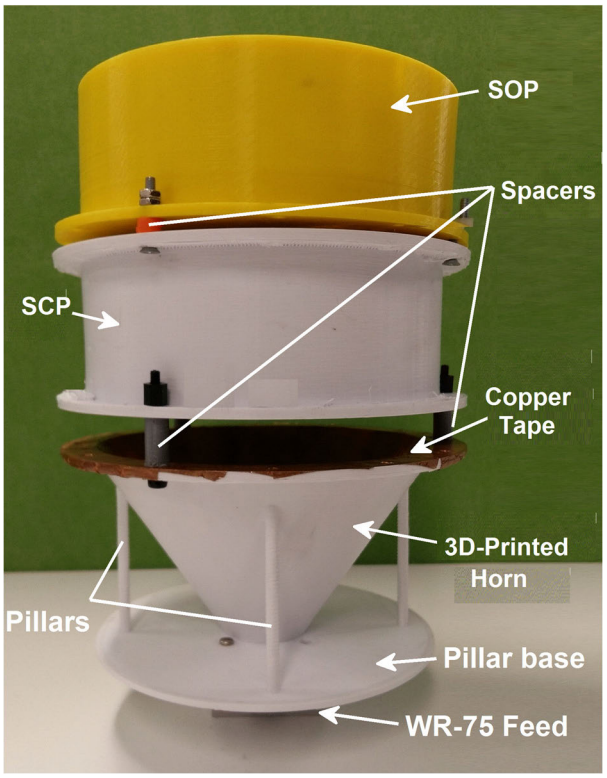

FIGURE 14. Photograph of the beam scanning system made with a horn antenna and pair of perforated dielectric structures.

printer, which were used for the fabrication of SCP and horn antenna. A picture of the fabricated and assembled antenna system prototype is shown in Fig. 14. In this prototype, made to experimentally prove the concept from electromagnetic perspective, a rotation mechanism was not implemented. To illustrate the acclimatization ability of modern additive manufacturing technique and for performance comparison,

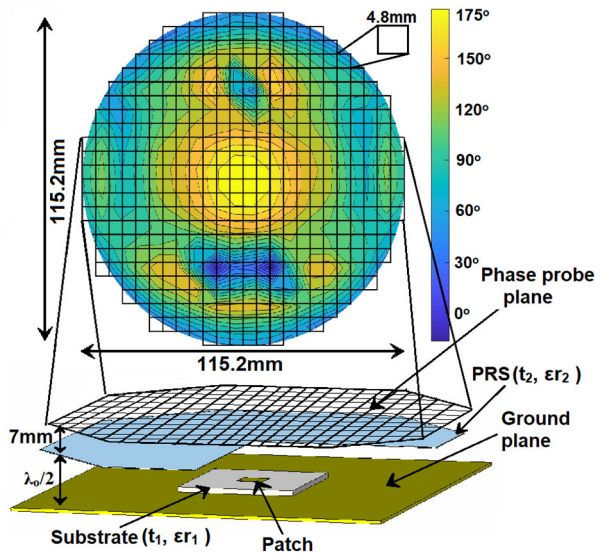

FIGURE 15. Phase of the H-plane electric field predicted on the aperture of RCA using full-wave electromagnetic simulations.

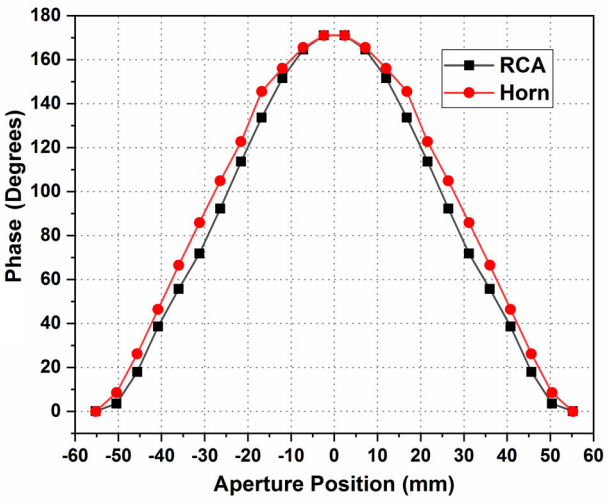

FIGURE 16. Comparison of phase distribution profiles of the horn antenna and RCA.

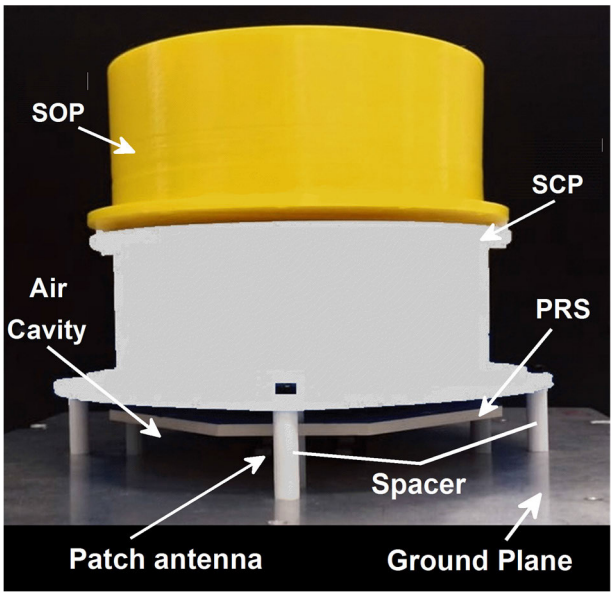

FIGURE 17. Photograph of Antenna System II composed of a low-profile RCA base antenna and a pair of PDSs.

System II was designed, which comprised of same PDS pair mounted on top of RCA, which is discussed in the following Section.

V. SYSTEM II: BEAM-STEERING SYSTEM WITH A RESONANT-CAVITY BASE ANTENNA

The RCA is a low- profile antenna comprising of a resonating cavity that is formed between the ground plane and a partially reflecting superstrate [35], [36]. The field bounces back and forth in the cavity and propagates in lateral directions, improving radiation performance due to increased effective aperture [37]. For the current application, an RCA was designed to operate at the design frequency of the previous SOP, i.e. 11 GHz. An octagonal-shaped partially reflecting surface (PRS), placed $\lambda_0/2$ ($\simeq$13.6 mm at the operating frequency) above the ground plane, formed the cavity, which is fed by a small microstrip patch antenna. The patch was printed on a Rogers UltraLam2000 slab (thickness (t_1) = 1.57 mm, ε_{r1} = 2.5) while the completely dielectric PRS was made up of Rogers TMM4 (t_2 = 3.175 mm, ε_{r2} = 4.5). The RCA configuration and phase distribution at the height 7 mm above the aperture is shown in Fig. 15. Maximum lateral dimension of the PRS is $4.2\lambda_0$ (=115.2mm), which is equal to the diameter of the SOP described in Section IV, Sub-Section *B*. This was done intentionally to use the same 3D-printed PDSs to steer the beam of the RCA. For this purpose, the aperture phase of RCA was probed at the height where its profile had closest match with that of horn. The comparison of phase for both base antennas is shown in Fig. 16. Complete beam scanning setup comprising of pair of SCP and SOP mounted on top of RCA is shown in Fig. 17. The results are explained in the next section.

VI. RESULTS AND DISCUSSION

Since beam-steering is achieved by rotating the two PDSs, we measured both systems for seven different rotation combinations of SCP and SOP. The SCP was fixed while SOP was rotated in the counter-clockwise direction in steps of 30°, i.e. $\alpha_1 = 0°$ and $\alpha_2 = 0°, 30° \ldots, 180°$. The rotation of SOP between 0° and 180°, while SCP is fixed to 0°, moves the beam peak from the furthest in elevation angle (maximum tilt) to the broadside direction following a spiral geometry.

Impedance matching of System I and System II were measured with an Agilent PNA-X N5242A network analyser and their radiation patterns were measured in an NSI spherical

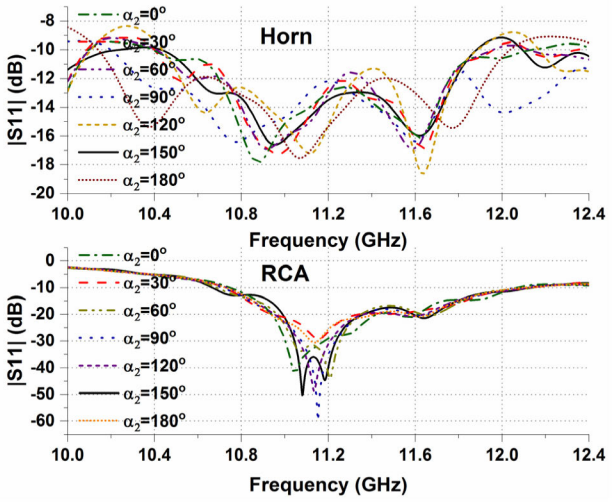

FIGURE 18. Dual panel showing 10dB return loss bandwidth for (a) horn antenna (b) RCA for different orientations of PDSs.

TABLE 5. Comparison of 10 dB return loss bandwidth of two antenna systems for different orientations of the PDS pair.

α_1 (Deg.)	α_2 (Deg.)	10 dB return loss bandwidth (%)	
		Horn Antenna	RCA
0°	0°	13.85	12.79
0°	30°	13.99	12.77
0°	60°	13.96	12.27
0°	90°	14.07	12.20
0°	120°	13.82	11.83
0°	150°	13.89	11.96
0°	180°	14.10	11.55

near-field anechoic chamber. The physical rotation of PDSs can affect the near-field distribution and thus potentially affect impedance matching, which could be detrimental to the overall efficiency of the system. To invalidate the hypothesis, we measured input reflection coefficients of both System I and System II for fourteen different configurations by rotating the SOP from 0° to 180° in steps of 30° while maintaining SCP stationary. The measured 10dB return loss bandwidth for both systems is listed in Table 5 and dual-panel plot is illustrated in Fig. 18. It is clearly depicted that both systems demonstrate an acceptable stability in impedance matching. System I, however has a slightly larger impedance bandwidth than System II in all the measured cases, which can be attributed to the inherent wideband matching of the conical horn used in System I.

The far-field patterns of both systems were also measured for the seven rotation combinations of SCP and SOP. The measured gain pattern cuts, taken at 11 GHz on a vertical plane that passes through the beam peak, are shown in Fig. 19(a) and (b) for all rotation angles of SOP. Each pattern cut is taken at a different azimuth angle containing the beam peak, which is indicated in the figure.

For both systems, the peak gain is within 3dB of the peak value and the highest side lobes are at least 5 dB below

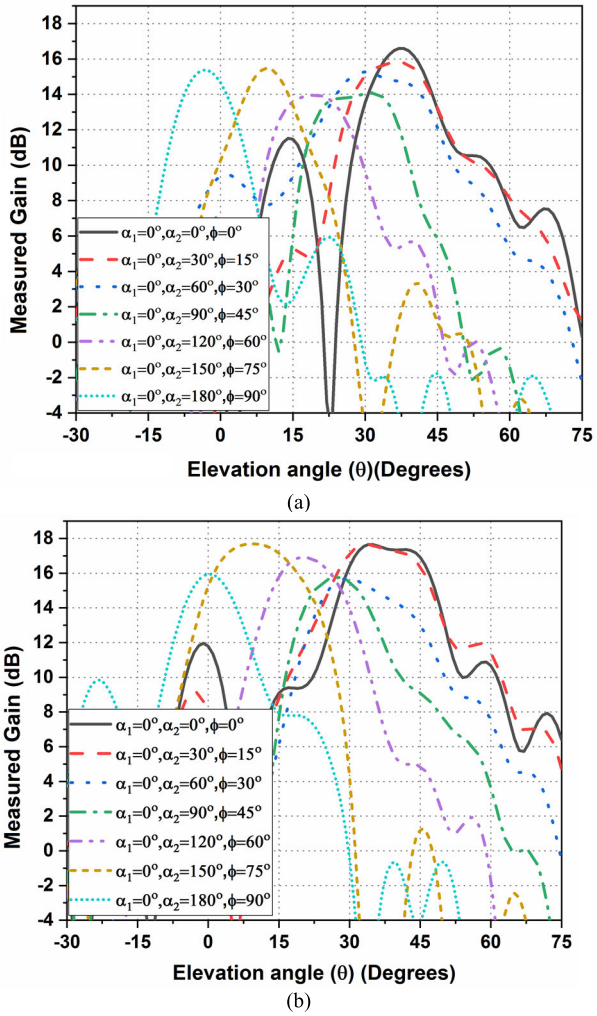

FIGURE 19. Measured elevation pattern cuts when SOP is rotated (α_2 is varied) and SCP is static ($\alpha_1 = 0°$) for (a) System I with a horn antenna, and (b) System II with an RCA.

the beam peaks. For System I, in Fig. 19(a), the maximum gain is 16.6 dBi when the beam is pointing at the elevation angle of 37°, which is also the maximum elevation steering angle of the system. The gain in the broadside direction is 15.4 dBi. The aperture efficiencies at maximum elevation steering angle and in broadside direction are 25.7% and 19.7%, respectively. For System II, in Fig. 19(b), the measured gain is 17.7 dBi at an elevation angle of 35°. The gain in the broadside direction is 16.0 dBi, and respective aperture efficiencies at maximum elevation steering angle and in broadside direction are 33.4% and 22.6%. The variation of measured gain when steering is interesting in both designs and is different to that observed in typical flat and non-tilting beam-steering antennas. In a typical electronically scanned phased array, the gain is highest in the broadside direction and lowest when the beam is furthest in the elevation plane, which is attributed to the reduction in the effective aperture for increased elevation angles [15]. The operating principle of the proposed antenna systems is to tilt beam through the linear phase shifts, progressively applied by the

TABLE 6. Broadside performance comparison of proposed systems with some of the recently reported designs.

Ref.	Measured Gain (dB)		Aperture area (λ_0^2)	Aperture Efficiency (%)	
	Broadside	Max. tilt		Broadside	Max. tilt
[39]	15.0	12.6	9.92	25.4	14.6
[40]	15.7	14.5	28.40	8.9	7.9
[41]	24.4	22.3	100.0	21.9	13.5
[15]	19.0	16.6	36.0	17.5	10.0
[40]	17.9	15.3	28.40	17.3	9.5
This work System I	15.4	13.8	13.95	19.7	13.6
This work System II	16.0	14.3	13.95	22.6	15.3

two PDSs in the propagating electric field. In the broadside steering case, the phase shift progression in the input electric field and phase progression through the SOS are opposite to each other which reduces its overall phase transformation efficiency. Nevertheless, the beam maintains gain value to a level achieved with systems design using commercial dielectric materials. A comparison of key performance parameters with most recent work on similar designs is given in Table 6, which summarizes peak gain, electrical size, aperture efficiency and difference between measured gains when the beam at the broadside and when it is at maximum elevation angle.

The use of low permittivity material to design PDSs results in large electric thicknesses and a portion of the electromagnetic energy exits through the thick edges of PDSs. The cross-sectional view of the E-field propagation of System II for $\alpha_2 = 120°$ is illustrated in Fig. 20. The radiation loss from the edges is evident, which results in reduced power in the desired beam. The severity of the edge effect reduces considerably by using a higher permittivity dielectric material for the PDSs, which reduces the height of the PDSs. To validate the hypothesis, we designed two PDSs using a dielectric material of relative permittivity 4.5, which decreases PDS thickness to 26 mm ($0.95\lambda_0$). These PDSs were integrated with the horn and the RCA base antenna models and simulated. Unlike the ABS based structures, the new antenna systems have more stable and higher broadside gains of 16.1dB with the horn base antenna and 17.3dB with RCA. It is pertinent to mention here that measured and theoretically calculated elevation angles for maximum tilt provided in Table 1 and Fig. 19 are not in agreement. This is attributed to the excessive height of the PDSs and can be rectified by reducing the overall height of the system. The edge effect of the PDSs is further analyzed by comparing the power exiting through planar surfaces of the PDSs to that of the base antenna in the following subsection.

A. RADIATED POWER ANALYSIS

To quantify power leakage through thick edges, we probed the total power exiting (a) the base antennas without PDSs, (b) the top surface of SOP without SCP, and (c) from the

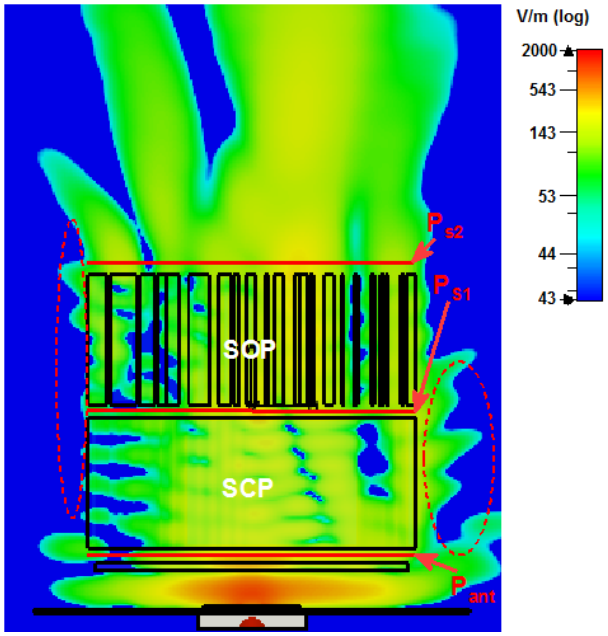

FIGURE 20. Maximum field amplitude of propagating dominant electric field at instantaneous phase of $3\pi/4$, when $\alpha_2 = 120°$. A strong field intensity can be seen leaking from the edges of the two dielectric structures.

top surface of the SCP in the complete steering system. The power is probed in three planes referred to as P_{ant}, P_{s1}, and P_{S2}, which are defined 0.5 mm above the base antenna, SCP, and SOP, respectively, as shown in Fig. 20. In these three planes equal-sized circular areas of diameter 124.8 mm have been considered for probing.

The total power flow passing through each surface was probed by creating a 2D grid of 4.8mm × 4.8mm cells. The dominant electric and magnetic field vector components were probed at the centre of each cell, which are then used to calculate the pointing vector (S) component in the z-direction and the total power through each surface using:

$$S_z = E_y \times H_x^* \tag{8}$$

$$P = \sum_1^n \left(\frac{1}{2}(S_n.\Delta A)\right) \tag{9}$$

where, ΔA is the area of each grid element, E_y is the dominant y-component of the electric field and H_x* is the conjugate of the dominant x-component of the magnetic field.

The total power probed in P_{ant} for System I and System II is 0.46 W and 0.47 W, respectively. Although the power at the antenna input port is 0.5W, we will use the power levels at P_{ant} for estimating the power percentage leaking out from the edges of the SCP and SOP. The power level in P_{s1} drops to 0.4 W in System I and 0.42 W in System II when SCP is placed above horn and RCA, respectively. This difference of P_{s1} and P_{ant} is the amount of power leaking from the sidewalls of SCP, which is 13% for System I and 10.6% for System II.

The power in P_{S2} for both systems are summarized for different rotation angles of SOP in Table 7. The trend of

TABLE 7. Total Radiated power in plane parallel to the antenna aperture at 11 GHz.

		Horn Power (Watt)	RCA Power (Watt)
Base Antenna		0.47	0.47
With SCP only		0.40	0.42
Antenna with SCP and rotating SOP			
α_1 (Deg.)	α_2(Deg.)		
0°	0°	0.36	0.39
0°	30°	0.36	0.39
0°	60°	0.35	0.39
0°	90°	0.34	0.38
0°	120°	0.34	0.38
0°	150°	0.35	0.39
0°	180°	0.36	0.38

variation in power levels is similar to the trend in the measured gain values observed in Fig. 19. As an example, at the operational frequency, System II has lowest power levels in P_{s2} and lowest peak directivity when $\alpha_2 = 90°$ and $\alpha_2 = 120°$.

B. WIDEBAND PERFORMANCE ANALYSIS

Apart from demonstrating beam-steering, one of the major motivation of this work was to investigate radiation performance in a frequency band around the center operating frequency. To compare the bandwidth and the angular coverage of the two designs, we represented the measured peak gain as contours on frequency vs. elevation angle plots for all seven orientations of PDSs in Fig. 21. For the comparison, the gain values within 3dB limit of the maximum gain of each systems are visible in these contours. The data along the horizontal axis presents the gain variation with increasing elevation angles at a fixed frequency while the data along the vertical axis presents gain variation in a wider frequency band and at a fixed elevation angle.

From the contour plots, it can be inferred that System II has a higher peak gain around the operating frequency. However, System I has larger 3dB gain bandwidth, which is evident from a bigger colored area of the plot. The bandwidth depends on the aperture phase variation of the base antenna and the phase delay provided by the SCP and SOP. Since the SCP and SOP are identical in the two systems, the larger gain bandwidth of System I can be attributed to more stable phase profile of the horn antenna versus frequency, relative to the RCA. Variations in gain and the aperture efficiency of the two antenna systems with frequency, at zero tilt, are given in Table 8.The system with horn antenna has lower but stable peak gain within the frequency band from 10.4 GHz to 11.8 GHz. The RCA based system has a higher peak gain and about 2dB variation in gain within the frequency range from 10.4 GHz and 11.0 GHz. Both antennas maintain gain values that comparable to closely related recently published antennas that have been implemented using more expensive commercial dielectric materials. A comparison of key performance parameters with some recent relevant work is given in

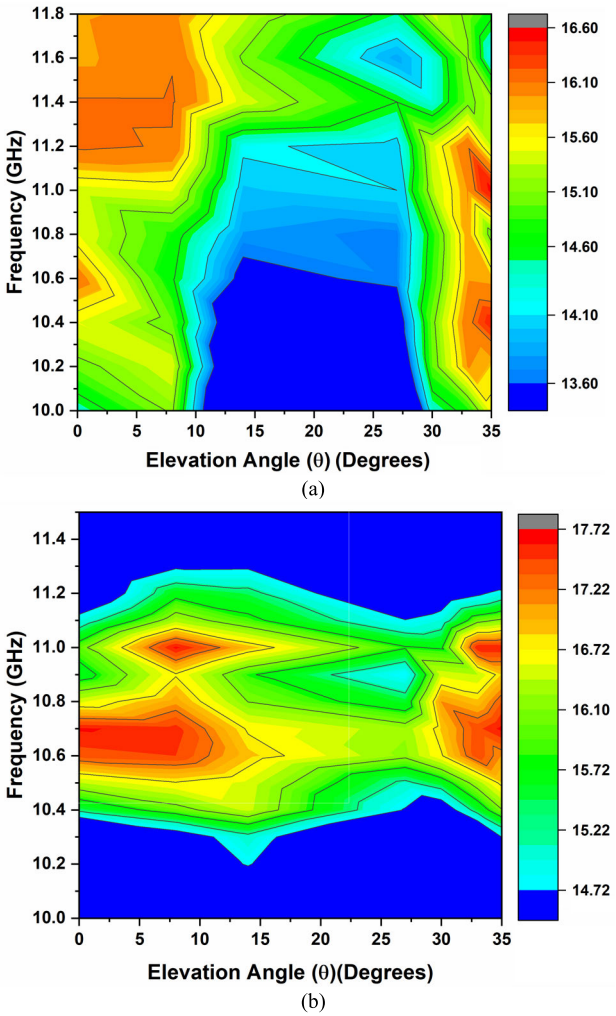

FIGURE 21. Measured realized gain at different elevation angles in a wider frequency band for (a) System I with a horn base antenna and (b) System II with RCA base antenna.

Table 6, which summarizes aperture area, measured antenna gains and aperture efficiencies when the beam at broadside and when it is at maximum elevation angle. To explain this further, we probed the phase of the dominant near-electric field component along H-Plane (xz-plane here) on the aperture of horn and RCA in a frequency band between 10 GHz and 15 GHz. The numerically obtained phase profile is presented with contours in Fig. 22 (a) and (b).

The horn antenna does not have abrupt variation in aperture phase distribution when compared with RCA. The phase of RCA is relative uniform in the frequency band between 10 GHz and 12 GHz but has larger variation beyond 12 GHz. The maximum phase variation in RCA aperture is about 170° between 10 GHz and 12 GHz but exceeds 290° in the frequency beyond 12 GHz. On the other hand, the maximum phase variation on horn aperture is not more than 170° throughout the frequency band between 10 GHz and 15 GHz. It is pertinent to mention here that the correction phase delay included in the SCP design in Section IV also has a maximum phase delay of 170°. Although, relative phase

TABLE 8. Broadband performance analysis of proposed designs.

Freq. (GHz)	Horn		Freq. (GHz)	RCA	
	Broadside Gain (dB)	Aperture efficiency (%)		Broadside Gain (dB)	Aperture efficiency (%)
10.4	15.5	22.3	10.4	15.3	21.5
10.6	16.0	24.3	10.5	16.4	27.2
10.8	15.5	20.7	10.6	17.4	33.6
11.0	15.4	19.7	10.7	17.7	35.3
11.2	16.2	22.6	10.8	16.5	26.3
11.4	16.1	21.7	10.9	15.5	20.5
11.6	15.8	19.4	11.0	16.0	22.6
11.8	15.8	18.9	11.1	14.9	17.2

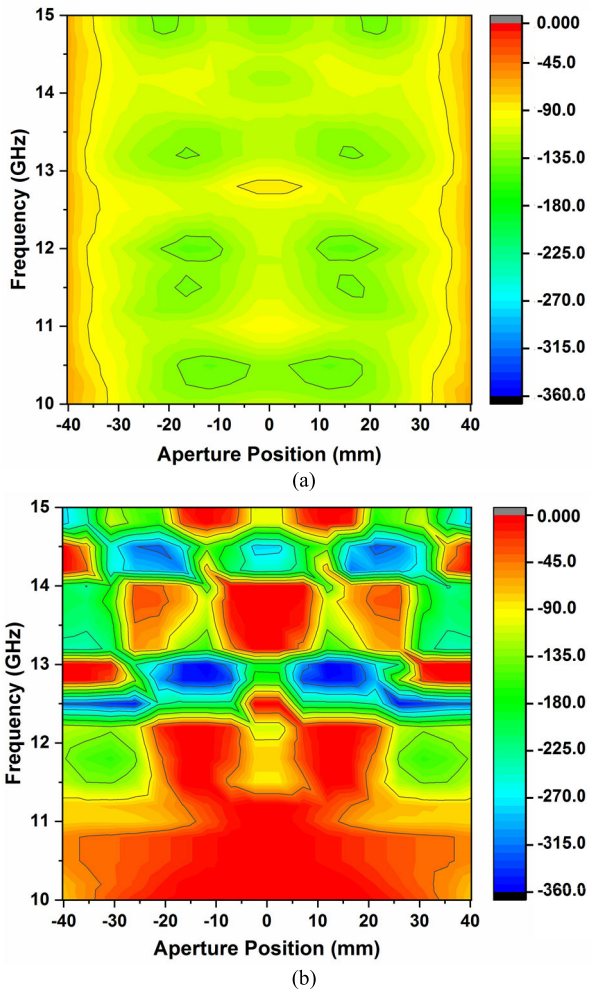

FIGURE 22. Wideband heatmap of aperture phase distribution in xz-plane for (a) Horn antenna (b) RCA.

distribution on the aperture is important to explain wideband phase transformation still maximum phase variation is a crude parameter to understand effectivity of SCP in a wider-band. To investigate this further, we calculated mean ($\bar{x}$) and standard deviation (s_x) for the aperture phase distributions of both horn and RCA, which are given in Fig. 23. It can be noted that mean ($\bar{x}$) and standard deviation (s_x) curve for horn antenna is almost flat in the frequency band between

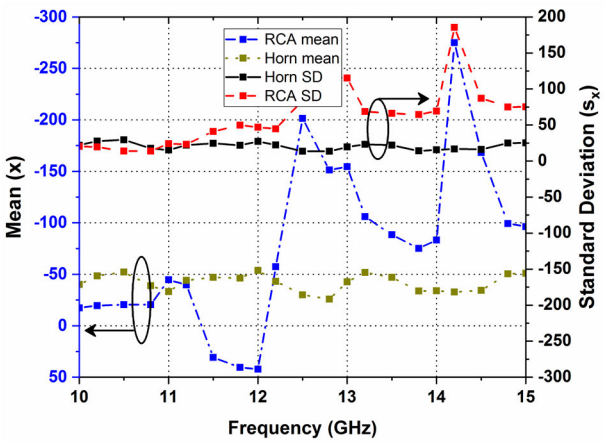

FIGURE 23. Mean and standard deviation of aperture phase distribution probed at varying frequencies in aperture planes on the conical horn and the RCA.

10 and 15 GHz. The RCA, on the other hand, has abrupt changes around 12 GHz. Thus the stability in aperture phase distribution of horn compared to RCA makes it more suitable for wideband applications.

Although the high gain value at a larger band makes both systems a perfect candidate for 5G communication but the design is not ideal. Modern RF-graded 3D-printable materials with higher dielectric constants such as PREPERM® ABS800, PREPERM® ABS1000, ABS1200 and ABS1500 help to reduce the individual heights of the SOP and SCP to 15.75 mm, 12.6 mm, 10.5 mm and 8.4 mm, respectively [36]. But the respective prices of a single spool of aforementioned materials in US$ are 620, 500, 350 and 320, respectively. At present, they are a lot more expensive compared to a commercial spool of ABS that costs US$ 16.30. But still they are economical compared to traditional dielectrics by many folds. Moreover, some high permittivity materials have printing complications and cannot be printed using common low-cost household printers. This is a trade-off between the design process and performance of the prototype, which is expected to reduce with the rapid advancement in 3D printing technology.

VII. CONCLUSION

Beam–steering antennas using physical rotation of a pair of 3D-printed perforated dielectric structures (PDSs) are presented. PDSs are developed at negligible cost when compared with multilayered printed metasurfaces. PDSs are also superior to dielectric wedges with saw-tooth type geometry and do not have mechanically weak regions that can cause structural failure in laterally large PDSs required for high-gain antennas. The PDSs can be used with different types of feed antennas that are appropriate for the application. The first prototype developed using a horn antenna has a peak gain of 16.6 dBi and bandwidth of 1.2 GHz. A second prototype developed using a resonant-cavity antenna (RCA) has a peak gain of 17.7 dBi and bandwidth of 0.7 GHz. Both antenna systems can steer the beam to a farthest elevation angle of

35°. The RCA based antenna system is 35.6% shorter than the horn-based system but has reduced bandwidth. The wideband scanning ability and low-fabrication cost of the demonstrated systems make them a suitable candidate to develop extremely low-cost consumer terminals for receiving upcoming satellite services. The main limitation of antennas realized using this method is due to relatively high RF losses and limited choice of dielectric constants of in inexpensive 3D printable materials that are commonly available at present. With expected rapid advancement in material technology, it will be possible to realize high performance, low-cost antenna systems using this method in the near future.

REFERENCES

[1] D. Rodrigo, L. Jofre, and B. A. Cetiner, "Circular beam-steering reconfigurable antenna with liquid metal parasitics," *IEEE Trans. Antennas Propag.*, vol. 60, no. 4, pp. 1796–1802, Apr. 2012.

[2] C. W. Baek, S. Song, J. H. Park, S. Lee, J. M. Kim, W. Choi, C. Cheon, Y. K. Kim, and Y. Kwon, "A V-band micromachined 2-D beam-steering antenna driven by magnetic force with polymer-based hinges," *IEEE Trans. Microw. Theory Techn.*, vol. 51, no. 1, pp. 325–331, Jan. 2003.

[3] C. R. Liu, S. Q. Xiao, Y. X. Guo, Y. Y. Bai, and B. Z. Wang, "Broadband circularly polarized beam-steering antenna array," *IEEE Trans. Antennas Propag.*, vol. 61, no. 3, pp. 1475–1479, Mar. 2013.

[4] I. Uchendu and J. R. Kelly, "Survey of beam steering techniques available for millimeter wave applications," *Prog. Electromagn. Res. B*, vol. 68, pp. 35–54, 2016.

[5] N. Ojaroudiparchin, M. Shen, S. Zhang, and G. F. Pedersen, "A switchable 3-D-coverage-phased array antenna package for 5G mobile terminals," *IEEE Antennas Wireless Propag. Lett.*, vol. 15, pp. 1747–1750, 2016.

[6] M. Mantash and T. A. Denidni, "Millimeter-wave beam-steering antenna array for 5G applications," in *Proc. IEEE 28th Annu. Int. Symp. Pers., Indoor, Mobile Radio Commun. (PIMRC)*, Oct. 2017, pp. 1–3.

[7] B. Yu, K. Yang, C.-Y.-D. Sim, and G. Yang, "A novel 28 GHz beam steering array for 5G mobile device with metallic casing application," *IEEE Trans. Antennas Propag.*, vol. 66, no. 1, pp. 462–466, Jan. 2018.

[8] A. Dreher, N. Niklasch, F. Klefenz, and A. Schroth, "Antenna and receiver system with digital beamforming for satellite navigation and communications," *IEEE Trans. Microw. Theory Techn.*, vol. 51, no. 7, pp. 1815–1821, Jul. 2003.

[9] M. U. Afzal and K. P. Esselle, "Application of near-field phase transformation to steer the beam of high-gain antennas in two dimensions," in *Proc. IEEE Int. Symp. Antennas Propag. USNC/URSI Nat. Radio Sci. Meeting*, Jul. 2017, pp. 1947–1948.

[10] R.-S. Chen, S.-W. Wong, G.-L. Huang, Y. He, and L. Zhu, "Bandwidth-enhanced high-gain full-metal filtering slot antenna array using TE101 and TE301 cavity modes," *IEEE Antennas Wireless Propag. Lett.*, vol. 20, no. 10, pp. 1943–1947, Oct. 2021.

[11] G. Q. Luo, Z. F. Hu, W. J. Li, X. H. Zhang, L. L. Sun, and J. F. Zheng, "Bandwidth-enhanced low-profile cavity-backed slot antenna by using hybrid SIW cavity modes," *IEEE Trans. Antennas Propag.*, vol. 60, no. 4, pp. 1698–1704, Apr. 2012.

[12] M. Nikfalazar, M. Sazegar, A. Mehmood, A. Wiens, A. Friederich, H. Maune, J. R. Binder, and R. Jakoby, "Two-dimensional beam-steering phased-array antenna with compact tunable phase shifter based on BST thick films," *IEEE Antennas Wireless Propag. Lett.*, vol. 16, pp. 585–588, 2017.

[13] G. D'Amato, G. Avitabile, G. Coviello, and C. Talarico, "DDS-PLL phase shifter architectures for phased arrays: Theory and techniques," *IEEE Access*, vol. 7, pp. 19461–19470, 2019.

[14] K. Singh, M. U. Afzal, M. Kovaleva, and K. P. Esselle, "Controlling the most significant grating lobes in two-dimensional beam-steering systems with phase-gradient metasurfaces," *IEEE Trans. Antennas Propag.*, vol. 68, no. 3, pp. 1389–1401, Mar. 2020.

[15] M. U. Afzal and K. P. Esselle, "Steering the beam of medium-to-high gain antennas using near-field phase transformation," *IEEE Trans. Antennas. Propag.*, vol. 65, no. 4, pp. 1680–1690, Apr. 2017.

[16] J. Canet-Ferrer, *Metamaterials Metasurfaces*. London, U.K.: IntechOpen, 2019.

[17] H. Li, C. Ma, F. Shen, K. Xu, D. Ye, J. Huangfu, C. Li, L. Ran, and T. A. Denidni, "Wide-angle beam steering based on an active conformal metasurface lens," *IEEE Access*, vol. 7, pp. 185264–185272, 2019.

[18] F. Ahmed, T. Hayat, M. U. Afzal, A. Lalbakhsh, and K. P. Esselle, "Dielectric-free cells for low-cost near-field phase shifting metasurfaces," in *Proc. IEEE Int. Symp. Antennas Propag. North Amer. Radio Sci. Meeting*, Jul. 2020, pp. 741–742.

[19] M. U. Afzal, L. Matekovits, K. P. Esselle, and A. Lalbakhsh, "Beam-scanning antenna based on near-electric field phase transformation and refraction of electromagnetic wave through dielectric structures," *IEEE Access*, vol. 8, pp. 199242–199253, 2020.

[20] A. A. Baba, R. M. Hashmi, K. P. Esselle, M. Attygalle, and D. Borg, "A millimeter-wave antenna system for wideband 2-D beam steering," *IEEE Trans. Antennas Propag.*, vol. 68, no. 5, pp. 3453–3464, May 2020.

[21] C. D. McEwen and M. R. Khan, "Beam steering method with improved sidelobe response using dielectric wedges for satellite TV reception," in *Proc. 14th Eur. Microw. Conf.*, Oct. 1984, pp. 681–685.

[22] H. D. Griffiths and M. R. Khan, "Antenna beam steering technique using dielectric wedges," *IEE Proc. H Microw., Antennas Propag.*, vol. 136, no. 2, pp. 126–131, Apr. 1989.

[23] M. R. Khan, "A beam steering technique using dielectric wedges," Ph.D. dissertation, Dept. Electron. Elect. Eng, Univ. London, London, U.K., 1995.

[24] T. Hayat, M. U. Afzal, A. Lalbakhsh, and K. P. Esselle, "Additively manufactured perforated superstrate to improve directive radiation characteristics of electromagnetic source," *IEEE Access*, vol. 7, pp. 153445–153452, 2019.

[25] J. Wang and Y. Ramhat-Samii, "Phase method: A more precise beam steering model for phase-delay metasurface based Risley antenna," in *Proc. URSI Int. Symp. Electromagn. Theory (EMTS)*, May 2019, pp. 1–4.

[26] M. U. Afzal, A. Lalbakhsh, and K. P. Esselle, "Electromagnetic-wave beam-scanning antenna using near-field rotatable graded-dielectric plates," *J. Appl. Phys.*, vol. 124, no. 23, Dec. 2018, Art. no. 234901.

[27] T. Hayat, M. U. Afzal, F. Ahmed, S. Zhang, K. P. Esselle, and Y. Vardaxoglou, "Low-cost ultrawideband high-gain compact resonant cavity antenna," *IEEE Antennas Wireless Propag. Lett.*, vol. 19, no. 7, pp. 1271–1275, Jul. 2020.

[28] A. Petosa and A. Ittipiboon, "Design and performance of a perforated dielectric Fresnel lens," *IEE Proc.-Microw., Antennas Propag.*, vol. 150, no. 5, pp. 309–314, Oct. 2003.

[29] A. M. Nicolson and G. F. Ross, "Measurement of the intrinsic properties of materials by time-domain techniques," *IEEE Trans. Instrum. Meas.*, vol. IM-19, no. 4, pp. 377–382, Nov. 1970.

[30] M. S. Pavlovic and B. M. Kolundzija, "Emulation of gain measurements of standard gain pyramidal horns using 3D EM solver," in *Proc. IEEE Int. Symp. Antennas Propag. (APSURSI)*, Jul. 2011, pp. 1906–1909.

[31] E. Canessa, C. Fonda, M. Zennaro, and N. Deadline, "Low–cost 3D printing for science, education and sustainable development," *Low-Cost 3D Printing*, vol. 11, no. 1, 2013.

[32] P. F. McManamon, P. J. Bos, M. J. Escuti, J. Heikenfeld, S. Serati, H. Xie, and E. A. Watson, "A review of phased array steering for narrow-band electrooptical systems," *Proc. IEEE*, vol. 97, no. 6, pp. 1078–1096, Jun. 2009.

[33] M. Q. Qi, W. X. Tang, H. F. Ma, B. C. Pan, Z. Tao, Y. Z. Sun, and T. J. Cui, "Suppressing side-lobe radiations of horn antenna by loading metamaterial lens," *Sci. Rep.*, vol. 5, no. 1, pp. 1–6, Aug. 2015.

[34] M. U. Afzal, K. P. Esselle, and B. A. Zeb, "Dielectric phase-correcting structures for electromagnetic band gap resonator antennas," *IEEE Trans. Antennas Propag.*, vol. 63, no. 8, pp. 3390–3399, Aug. 2015.

[35] T. Hayat, K. P. Esselle, M. U. Afzal, and K. Singh, "3D printed all dielectric phase correcting surface for resonant cavity antenna," in *Proc. IEEE Asia–Pacific Conf. Antennas Propag. (APCAP)*, Aug. 2018, pp. 214–215.

[36] T. Hayat, M. U. Afzal, A. Lalbakhsh, and K. P. Esselle, "3-D-printed phase-rectifying transparent superstrate for resonant-cavity antenna," *IEEE Antennas Wireless Propag. Lett.*, vol. 18, no. 7, pp. 1400–1404, Jul. 2019.

[37] A. P. Feresidis and J. C. Vardaxoglou, "High gain planar antenna using optimised partially reflective surfaces," *IEE Proc.-Microw., Antennas Propag.*, vol. 148, no. 6, pp. 345–350, Dec. 2001.

[38] S. J. Orfanidis, "Electromagnetic waves and antennas," Dept. ECE, Rutgers Univ., Piscataway, NJ, USA, 2002, pp. 163–166.
[39] M. E. Trampler, R. E. Lovato, and X. Gong, "Dual-resonance continuously beam-scanning X-Band reflectarray antenna," *IEEE Trans. Antennas Propag.*, vol. 68, no. 8, pp. 6080–6087, Aug. 2020.
[40] Q. Zeng, Z. Xue, W. Ren, W. Li, and S. Yang, "Beam-steering lens antenna using two transmit arrays at X-band," in *Proc. IEEE Asia–Pacific Microw. Conf. (APMC)*, Dec. 2019, pp. 1212–1213.
[41] H. Luyen, Z. Zhang, J. H. Booske, and N. Behdad, "Wideband, beam-steerable reflectarrays based on minimum-switch topology, polarization-rotating unit cells," *IEEE Access*, vol. 7, pp. 36568–36578, 2019.

TOUSEEF HAYAT (Student Member, IEEE) received the B.S. degree in telecommunication engineering from the University of Engineering and Technology, Taxila, Pakistan, the M.S. degree (Hons.) from the National University of Sciences and Technology (NUST), Islamabad, Pakistan, and the Master of Research (M.Res.) degree (Hons.) in electronics engineering from Macquarie University, Australia, in 2018, where he is currently pursuing the Ph.D. degree. His research interests include electromagnetic-bandgap resonant antennas, additive manufacturing of microwave components, phase and amplitude transforming metasurfaces, and dielectric characterization. He received several prestigious awards, including the International Research Training Program Scholarship (iRTP) for the MRes and the International Macquarie University Research Excellence Scholarship (iMQRES) for his Ph.D. degree.

MUHAMMAD U. AFZAL (Senior Member, IEEE) received the bachelor's degree in electronics engineering and the master's degree in computational science and engineering from the National University of Sciences and Technology (NUST), Islamabad, in 2009 and 2011, respectively, and the Ph.D. degree in electronics engineering from Macquarie University, Australia, in 2017. His doctoral research led to two breakthroughs in the field of electromagnetics and antennas. He has been working in the field of electromagnetics and antennas for more than ten years. In 2010, he started his career as a Lab Engineer at the Research Institute for Microwave and Millimetre-Wave Studies (RIMMS), NUST. In 2012, he was promoted to the position of a Lecturer, which he continued till February 2013. In 2017, after the Ph.D. degree, he was offered a postdoctorate for three years on a project funded by the Australian Research Council (ARC) through the Discovery Grant Scheme at Macquarie University. He is currently working as a Research Fellow at the University of Technology Sydney. He is an Active Researcher and has been publishing more than ten research papers each year and also involved in research supervision. In the last five years, he has co-supervised five Ph.D., three master's of research, and several undergraduate thesis students. His work on near-field phase-correction is a game-changing practical design approach to develop low-profile high-gain antennas as this method uses actual electric field (vectors) phase and not the ray tracing technique, traditionally used in phase-correcting lenses. The method provides freedom to a designer in performing phase correction at a distance as close to as half of the free-space wavelength spacing from antenna, which is traditionally performed in the far-field regions or at least three to five wavelengths spacing. His second contribution is the development of near-field meta-steering (NFMS) technology, which is an IP protected invention. This technology yields beam-steering antenna systems that are superior to both electronically steered active phased arrays and all mechanically steered/tilted reflector dishes or flat panel antennas. His innovative work on beam-steering technology received the "Highly Commended" certificate in the Five Future-Shaping Research Priorities category in the 2017 Academic Staff Awards at Macquarie University.

FOEZ AHMED (Student Member, IEEE) received the B.Sc. (Hons.) and M.Sc. degrees in information and communication engineering from the University of Rajshahi (RU), Bangladesh, in 2007 and 2009, respectively, and the M.Eng. degree in electrical and computer engineering from the South China University of Technology (SCUT), China, in 2013. He is currently pursuing the Ph.D. degree with the School of Electrical and Data Engineering, University of Technology Sydney (UTS), Sydney, Australia.

From 2012 to 2014, he was a Lecturer with the Department of Information and Communication Engineering, RU, where he has been working as an Assistant Professor (now on study leave), since 2014. He was also a Lecturer at the Northern University of Bangladesh, Dhaka, Bangladesh, from 2008 to 2009; and King Khalid University, Abha, Saudi Arabia, from 2009 to 2011. His current research interests include high-gain antennas, SATCOM antennas, metasurfaces, frequency selective surfaces, and far-field pattern synthesis using near-field phase transformation.

Mr. Ahmed was a recipient of several prestigious awards and scholarships, including the Commonwealth-Funded International Research Training Program (iRTP) Scholarship; the International Research Scholarship (IRS) and the Faculty of Engineering and Information Technology (FEIT) Scholarship from the University of Technology Sydney, Australia; the Gold Medal from RU; the Chinese Government Scholarship; the Academic Achievement Award; and the Excellency Award, SCUT, China.

SHIYU ZHANG (Member, IEEE) received the M.Sc. degree from The University of Manchester, Manchester, U.K., in 2010, and the Ph.D. degree from Loughborough University, Loughborough, U.K., in 2014.

Following graduation, he worked as a Research Associate with Loughborough University, where he is currently with the Wolfson School of Mechanical, Electrical and Manufacturing Engineering. He carried out research on additive manufacturing 3-D antennas and metamaterials. His current research interests include additive manufacturing (3-D-printing) antennas and RF circuit components, metamaterials, heterogenous artificial dielectrics, and wearable antennas and electronic systems.

Dr. Zhang received the EPSRC Doctoral Prize Research Fellowship Award, in 2015.

KARU PRIYATHAMA ESSELLE (Fellow, IEEE) received the B.Sc. degree (Hons.) in electronic and telecommunication engineering from the University of Moratuwa, Sri Lanka, and the M.A.Sc. and Ph.D. degrees with near-perfect GPA in electrical engineering from the University of Ottawa, Canada. He is currently a Distinguished Professor in electromagnetic and antenna engineering at UTS. Previously, he was the Director of the WiMed Research Centre and the Associate Dean of Higher Degree Research (HDR) with the Division of Information and Communication Sciences and directed the Centre for Collaboration in Electromagnetic and Antenna Engineering, Macquarie University. He has also served as a member for the Dean's Advisory Council and the Division Executive and the Head for the department several times. He has authored over 650 research publications and his papers have been cited ∼11,000 times. His H-index is 51 and i10 is 191. In 2020, his publications received over 1250 citations. Since 2002, his research team has been involved with research grants, contracts, and Ph.D. scholarships worth over 20 million dollars, including 15 Australian Research Council grants, without counting the 245 million-dollar SmartSat Corporative Research Centre, which started in 2019. His research has been supported by many national and international organizations, including Australian Research Council, Intel, U.S. Air Force, Cisco Systems, Hewlett-Packard, Australian Department of Defence, Australian Department of Industry, and German and Indian governments. He is a fellow of the Royal Society of New South Wales and Engineers Australia. He is the 2020 Runner-up to Australia's National Eureka Awards for Outstanding Mentor of Young Researchers. The 2019 Special Report on Research published by The Australian national newspaper selected him as the Research Field Leader in Australia in both electromagnetism and microelectronics. His other accolades, include the 2020 IEEE New South Wales Outstanding Volunteer Award, the 2019 Motohisa Kanda Award (from IEEE USA) for the most cited paper in IEEE TRANSACTIONS on EMC in the past five years, the 2019 Macquarie University Research Excellence Award for Innovative Technologies, the 2019 ARC Discovery International Award, the 2017 Excellence in Research Award from the Faculty of Science and Engineering, the 2017 Engineering Excellence Award for Best Innovation, the 2017 Highly Commended Research Excellence Award from Macquarie University, the 2017 Certificate of Recognition from IEEE Region 10, the 2016 and 2012 Engineering Excellence Awards for Best Published Paper from IESL NSW Chapter, the 2011 Outstanding Branch Counsellor Award from IEEE Headquarters (USA), the 2009 Vice Chancellor's Award for Excellence in Higher Degree Research Supervision, and the 2004 Innovation Award for Best Invention Disclosure. His mentees have been awarded many fellowships, awards, and prizes for their research achievements and 55 international experts, who examined the thesis of his recent Ph.D. graduates ranked them in the top 5% or 10%. In addition to the large number of invited conference speeches, he has been an Invited Plenary/Extended/Keynote Speaker of several IEEE and other conferences and workshops, including GSENN 2022, Denmark; EEEMEET 2022, Dubai; EuCAP 2020 Copenhagen, Denmark; URSI'19 Seville, Spain; and 23rd ICECOM 2019, Dubrovnik, Croatia.

J. (YIANNIS) VARDAXOGLOU received the B.Sc. degree in mathematics (mathematical physics) and the Ph.D. degree from the University of Kent at Canterbury, in 1981 and 1985, respectively.

He joined the Loughborough University of Technology, in 1988, as a Lecturer, promoted to a Senior Lecturer, in January 1992, and awarded the Personal Chair, in 1998. He was the Head and the first Dean of the Electronic, Electrical and Systems Engineering School, Loughborough University, from 2006 to 2012. He established the Wireless Communications Research (WiCR) Group, Loughborough University, and founded the Centre for Mobile Communications Research. He has pioneered research, design, and development of frequency selective surfaces (FSS) for communication systems, metamaterials, and low SAR antennas for mobile telephony, and has commercially exploited a number of his innovations. He has served as a Consultant for various industries and holds five patents. He is the Technical Director/the Founder of Antrum Ltd. (a University spinout company). He has attracted research funding from industry and has been awarded 20 EPSRC/EU research grants. He has published over 250 refereed journals and conference proceeding papers and written a book on FSS.

Dr. Vardaxoglou is a member of the EPSRC College in ICT and chaired the Executive Committee of Metamorphose and the EU FP6 NoE on Metamaterials. He is a fellow of the Institution of Engineering and Technology (FIET) and the Royal Academy of Engineering (FREng). He was the General Chair of EuCAP'2007. He was the past Chairperson of the Executive Committee of the IET's Antennas and Propagation Professional Network, U.K., and he chaired for five years the IEEE's Distinguish Lecturer Program of the Antennas and Propagation Society. He has chaired numerous IEE/IET events and has been with the Steering Committee of the IEE International Conferences on Antennas and Propagation and EuCAP'2006. He founded the Loughborough Antennas and Propagation Conferences (LAPC), which has been running, since 2005, where he is the Series Chair. He is a Chartered Engineer.